A high-resolution two-dimensional imaging velocimeter

P. M. Celliers,[a] D. J. Erskine, C. M. Sorce, D. G. Braun, O. L. Landen, and G. W. Collins
Lawrence Livermore National Laboratory, P.O. Box 808, Livermore, California 94551, USA

(Received 23 October 2009; accepted 17 January 2010; published online 10 March 2010)

Velocity interferometers are typically used to measure velocities of surfaces at a single point or along an imaged line as a function of time. We describe an optical arrangement that enables high-resolution measurements of the two-dimensional velocity field across a shock front or shocked interface. The technique is employed to measure microscopic fluctuations in shock fronts that have passed through materials being considered as ablators for indirect-drive inertial confinement fusion. With picosecond time resolution the instrument captures velocity modes with wavelengths as short as 2.5 μm at a resolution of $\sim$10 m/s rms on velocity fields averaging many km/s over an 800 μm field of view. © *2010 American Institute of Physics.* [doi:10.1063/1.3310076]

I. INTRODUCTION

There is much current interest in shock physics involving heterogeneous flow conditions. Heterogeneous flows are associated with the onset of plastic flow and failure in brittle and/or high strength materials,[1–3] with shock-induced phase transformations,[4] and with wave propagation through nonuniform media.[5,6] In these situations the wave profile and flow field are heterogeneous on microscopic and mesoscopic scales. One of the primary diagnostic tools in this field is velocity interferometry and, in particular, the Velocity Interferometer System for Any Reflector (VISAR) configuration of Barker and Hollenbach.[7,8] In velocity interferometry the Doppler velocity of a laser illuminated target is measured through a shift in phase of a fringe. The standard VISAR optical arrangement measures the fringe at a single point, or an array of discrete points, using high speed photodetectors and a quadrature phase decoding scheme.[9] More recently, an optical arrangement has been developed to produce fringe measurements along an imaged line using a streak camera as a detector.[10–12] With zero or one spatial dimension, current VISAR diagnostics provide only limited information on the three-dimensional character of heterogeneous flows. A two-dimensional (2D) spatial velocity field would provide important new information for many topics in shock wave research, because it would provide key information on spatial correlations in heterogeneous flows. In particular, our motivation for obtaining a 2D velocity field is driven by an important application in inertial confinement fusion[13] (ICF), in which there is a need to characterize small nonuniformities in shock-compressed ablator materials. Here, we present a demonstration of a picosecond-resolved snapshot of a spatial 2D velocity field such as produced behind a nonuniform shock front.

In the current ICF application the shock is created by the radiatively driven ablation of a capsule made from one of three candidate materials: Ge-doped CH, Cu-doped Be, or chemical vapor deposited diamond (CVD-C).[14] In ICF the shock passes through the ablator then into a layer of deuterium-tritium fuel. Nonuniformities in the ablator and/or heterogeneous flow behind the shock front will act as seed perturbations that are amplified by the Rayleigh–Taylor instability during the acceleration and deceleration phases of the capsule implosion. Multidimensional numerical studies of the implosion process indicate that flow nonuniformities greater than a few $\times$10 m/s rms at wavelengths as short as a few micrometers behind the initial shock will lead to enough instability growth to quench ignition of the fuel. In the case of the Be and CVD-C the shock cannot be probed directly through optical means. However, we can measure the degree of heterogeneity accumulated behind the initial shock front by transmitting the shock from the ablator material into a transparent layer of polymethylmethacrylate (PMMA) and probing the transmitted shock front just after it exits the ablator. The shock transmitted into the PMMA, moving at $\sim$20 km/s, is ionized and optically reflecting, acting as a mirror; quantitative probing of this "mirror" surface provides information about the heterogeneity of the flow behind it.

II. CONCEPT

In a traditional VISAR the optical interferometer has fixed delay τ between its arms. Doppler shifts in the beam passing through the interferometer are manifested as phase shifts in the interference fringes produced by the interferometer. The phase shift is proportional to $\tau\Delta\nu$, where $\Delta\nu$ is the frequency shift and τ is the interferometer delay time. In order to produce fringes with good visibility, the coherence length of the illumination source must be at least as large as τ, which in practice ranges up to several nanoseconds. Consequently VISARs are typically illuminated with narrow band single longitudinal mode (SLM) laser sources, with coherence times as long as the illumination pulse (tens of nanoseconds or longer).

VISAR interferometers are intrinsically capable of operating in an imaging mode with the fringe pattern superimposed on an image carried in the reflected beam.[10–12] In principle, a time-resolved 2D snapshot measurement of the

[a]Author to whom correspondence should be addressed. Electronic mail: celliers1@llnl.gov.

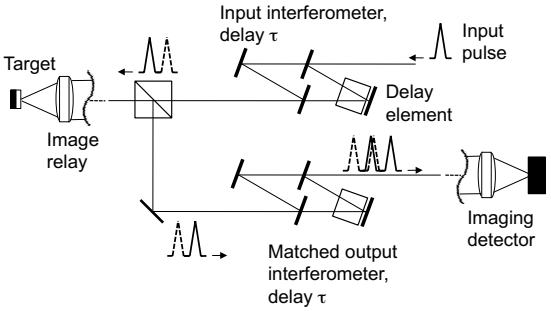

FIG. 1. Conceptual sketch (simplified) of the 2D VISAR illumination scheme. The input interferometer, illuminated by a picosecond pulse, produces two pulses separated by delay τ that are reflected from the target. The output interferometer with matching delay τ produces two pulses from each the returning input pulses, two of which are overlapped spatially and temporally at the detector to produce the interference.

velocity field could be collected using a SLM laser illuminating a standard imaging VISAR coupled to a fast framing detector.[5] However, to meet the resolution requirements of our ICF application, the framing detector must meet simultaneously the following requirements: gating time <100 ps over the whole field, array size of at least 700×700 pixels, and dynamic range >1000; a recording device that meets these requirements does not exist. Since a scientific grade charge-coupled device (CCD) detector meets most of the requirements with the exception of fast gating, it can be combined with a short illumination pulse (e.g., picosecond duration) to provide the time-resolved snapshot. As described above, however, the picosecond illumination pulse is incompatible with traditional VISAR systems because its coherence length is limited to the pulse duration. Expressed another way, a 1 ps pulse passed through a VISAR interferometer with $\tau\gg1$ ps will produce no interference. Thus, achieving high resolution 2D time-resolved fringes is not obvious at first glance.

The solution is to combine a picosecond illumination source and a time integrating CCD detector with the white light VISAR arrangement first described by Erskine and Holmes.[15,16] The white light VISAR arrangement provides a generic way to produce interference in a VISAR interferometer using a short coherence length light source. The idea is to prepare the input illumination by imprinting a coherent echo with time delay τ_s onto the illuminating beam before it interacts with the target. The reflected light from the target is then observed after passing through a second interferometer with time delay τ_d. The second interferometer will produce fringes (up to 50% visibility) when the two times τ_s and τ_d are matched to within a coherence length of the source illumination. In practice it is relatively easy to match the delays to within a few optical periods (few wavelengths of path difference), so that fringes can be produced with *any* broadband light source, e.g., tungsten lamp, light-emitting diode, or picosecond laser pulse.

To understand the white light VISAR with picosecond pulse illumination, follow the pulse through the system as it splits and recombines. A conceptual sketch of our optical arrangement, illustrated in Fig. 1, contains a pair of matched-delay velocity interferometers with the target placed between. The first interferometer, upstream of the target, divides the illumination pulse into a pair of pulses separated by time delay τ. These pulses, reflected by the target, pass through the second interferometer with matching delay τ, and are split again to produce four pulses. Two of the four returning pulses interfere because they have matching total path delay (overlapped in time and space at the detector). However, because the interfering pair interacted with the target at two different times separated by the interval τ, the phase encoded in the interference pattern is proportional to the local displacement of the reflecting surface $\Delta Z(x,y)$ that occurred over the interval τ, i.e., proportional to average velocity $\langle V(x,y)\rangle=\Delta Z(x,y)/\tau$. This information is spatially resolved over the transverse coordinates x and y of the image. The remaining two pulses do not interfere because they are not overlapped with any of the other pulses; they contribute only to the average intensity in the output image, thus the maximum fringe visibility is 50%. The velocity sensitivity is given by the usual expressions for the velocity-per-fringe (VPF) proportionality of a VISAR.[7,8,12] Thus the velocity calibration is as precise and accurate as for a traditional VISAR. A description with more mathematical detail is given in the Appendix.

III. IMPLEMENTATION

The optical implementation of our white-light VISAR is designed to operate at 395 nm, using the frequency-doubled ~1 mJ, 2 ps duration output of a commercial Ti:sapphire laser system. The imaging system was configured as a cascaded relay in which the imaging beams are passed through the interferometers similar to line-VISAR arrangements described previously.[12] It employs mostly commercial off-the-shelf parts and produces near diffraction-limited imaging performance at the detector over an 800 μm field of view and a F/3 collection aperture. The mode-locked oscillator of the picosecond-laser source was configured to have a round trip period that matched the period of the master clock of the shock driving laser and was phase locked to ensure accurate and stable timing of the probe relative to the shock driver. We determined the timing of the probe pulse relative to the shock breakout to an accuracy of ±20 ps using a streak camera to record the thermal emission observed upon breakout of the shock from the ablator into the PMMA layer, along with a fiducial of the probe signal; the latter was relayed to the streak camera through a fiber loop with an optical path matched to the imaging path. Target thermal emission on the CCD detector was eliminated by careful choice of the system bandpass (optical coatings and filters) and the use of fast mechanical shutters.

In our design the output interferometer employs a quadrature readout scheme as implemented in the first VISAR (Ref. 7) and improved upon by Hemsing.[9] Using polarizing optics the scheme produces four outputs and the phase of each output is shifted by 90° relative to its neighbor (analogous to phase stepping arrangements). By recording and algebraically manipulating all four outputs, it is possible to extract the phase at each point on the image independently of the neighboring points. Direct summation of the four

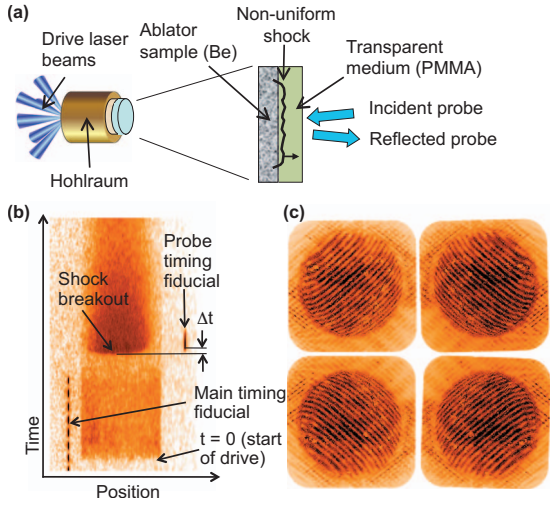

FIG. 2. (Color) (a) Sketch of the experimental package, (b) streak camera record showing the timing of the snapshot relative to the shock breakout, and (c) example of a four-frame interferogram formed from the reflection of the pulse pair from the shock front after passing through the sample. The square apertures in each frame are 900 μm across, and the circular shocked region has a diameter of 700 μm.

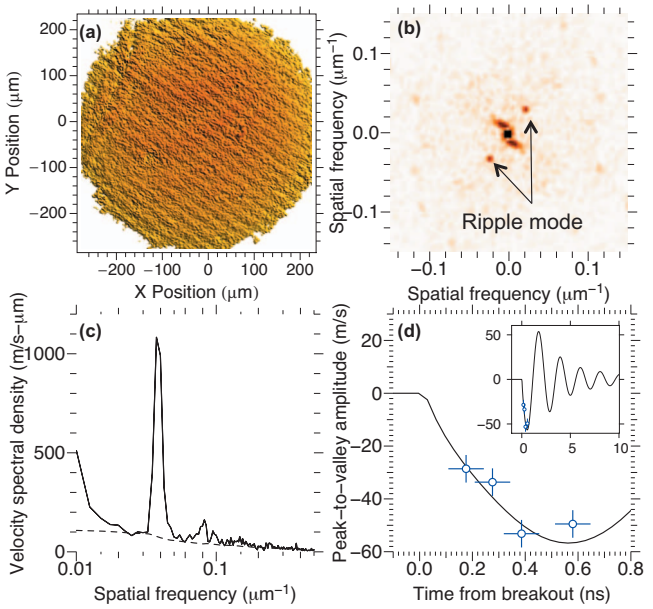

FIG. 3. (Color) (a) Surface rendering of the velocity data extracted from the data set of Fig. 2, (b) 2D power spectrum of the velocity showing the ripple modes, (c) one-dimensional lineout passing through the ripple mode (solid) compared to the noise floor (dashed), and (d) comparison of ripple mode amplitudes (open circles) with predictions from simulations (solid curve).

frames also produces the image of reflected light intensity (with no fringes). In our system the four-frame set is recorded on a large-frame Kodak 16801-E sensor with 4096×4096 pixels over a 36×36 mm^2 active area (9 μm pixels).

The 10 m/s sensitivity required for tests of ICF ablator materials can be connected to some basic spatial and temporal scales. It is well known that a nonuniform (rippled) shock in a homogeneous medium oscillates with period $T\sim\lambda_R/V$, where $V\sim20$ km/s is the shock velocity and λ_R is the transverse wavelength of the ripple mode.[17,18] Hydrodynamic simulations of our experimental conditions (a Be/PMMA interface) find $T=1.8\ \lambda_R/V$. Observable perturbation wavelengths range from 2.5 to 200 μm (the lower limit is the optical resolution limit), yielding T ranging from 0.25 to 20 ns, respectively. For steady velocities VISARs can be made increasingly sensitive by increasing the delay τ; however, the sensitivity to an oscillating signal decreases significantly when $\tau>T/2$. Therefore we kept $\tau\leq200$ ps to maintain sensitivity for $\lambda_R>4$ μm.

IV. RESULTS AND DISCUSSION

As a test of our system we fielded several targets consisting of uniformly doped Be samples that were fabricated with sinusoidal-shaped grooves of 25 μm period and 125 nm amplitude embedded into the ablator-PMMA interface. The sinusoidal perturbation is transferred to the shock front, which then undergoes a damped oscillation. The shock wave of amplitude around 360 GPa was produced by a thermal x-ray source characterized by a blackbody temperature of approximately 85 eV. The source was produced by irradiating the interior of a hohlraum target with 2 kJ of ultraviolet laser light from the OMEGA laser facility.[19] Figure 2(a) shows a sketch of the experimental package: a 2.7 mm diameter by 2 mm long Au hohlraum irradiated through a 1.6 mm diameter laser entrance hole on one end; a 900 μm hole on the opposite end exposed the sample package to the cavity radiation in order to drive the shock. The arrival time of the shock at the ablator-PMMA interface was monitored with a streak camera [data shown in Fig. 2(b)], which also recorded a timing fiducial that indicated the timing of the picosecond probe pulse relative to the shock breakout event. Figure 2(c) shows an example of the four-frame interferogram taken with interferometer delay $\tau=132.5$ ps at time 180 ps after the shock breakout. To aid with data analysis we imposed a background fringe field, which is subtracted during data analysis (discussed in more detail below). The imposed ripple perturbation is not apparent in the raw data because its amplitude is much smaller than a fringe.

When the fringe phase is extracted to construct a velocity map, in Fig. 3(a), the velocity ripple emerges clearly. Figure 3(b) shows the 2D power spectrum of the data in Fig. 3(a), revealing the ripple mode clearly, as the pair of peaks identified in the figure. Figure 3(b) also shows a diffuse low frequency pattern in the power spectrum. This pattern is an artifact that arose from a slight defect in the target package design.[20] Figure 3(c) shows a one-dimensional radial profile taken through the 2D power spectrum passing through the ripple mode at 0.04 μm^{-1} spatial frequency. One can determine the instantaneous velocity amplitude of the ripple signal by summing over the Fourier components occupied by the mode. Also shown in Fig. 3(c) is the spectrally resolved background noise (dashed curve) that will be discussed further below. It is clear that most of the observed spectrum is close to the background level (aside from the artifact mentioned above), while the ripple mode emerges well above the noise floor. To verify the time dependence of the ripple oscillation, four different experiments probed the target at different times relative to the shock breakout. The perturbation amplitudes extracted from the spectra of the measurements

are plotted in Fig. 3(d). From these plots the imposed modulations (peaking near 55 m/s peak-to-valley velocity difference) rise significantly above the noise spectrum at these frequencies. The vertical error bars in Fig. 3(d) correspond to the ±5 m/s peak-to-valley level of the noise spectrum summed (in quadrature) over the frequency bins occupied by the ripple mode. Hydrodynamic simulations, analytical calculations,[18] and simple estimates[21] of the velocity oscillation expected from these experiments are in good agreement.

The raw phase distribution contains a background phase and fixed pattern variations, which have to be characterized during experiments by recording a reference interferogram (from the stationary undriven target) a few moments prior to the shot. The reference phase is subtracted from the measured phase to produce the shot data. To characterize the noise inherent in this measurement process, we recorded a series of several blank interferograms returned from stationary targets. Since the target is stationary, the target contribution to the phase is ideally zero across the entire field. Therefore, in a noise-free environment one should be able to subtract any pair of the stationary target phases to produce a null, or zero phase difference. In practice the phase patterns produced by these tests varied randomly at a residual level, and any pair could never be subtracted to produce a null with amplitude below a well-defined noise floor. The spatial frequency spectra of multiple such tests produced a common spectral distribution (in a statistical sense) as shown by the dashed curve in Fig. 3(c). The observed residual rms phase fluctuation of the test nulls (quadrature summation over all modes) was $\delta\phi \sim 100$ mrad, equivalent to ~6.5 nm rms in OPD, or about $\lambda/60$. This defines the noise floor of the present system.[22] Translation of the $\lambda/60$ rms noise floor to velocity space requires knowledge of the VPF setting (etalon delay): with VPF=618 m/s/fringe (for $\tau=200$ ps), the $\lambda/60$ rms noise level corresponds to 10 m/s rms, or $\delta V/V \sim 5\times10^{-4}$ rms for a $V=20$ km/s shock front.

We attributed the dominant source of the residual noise to random fluctuations in the refractive index of the air paths internal to the two interferometers. Within these paths (total path ~1 m) the pulse pair travels through separated air columns. From shot to shot the relative OPD within these separated segments varies randomly at a level of $\sim 1:10^{-8}$. The magnitude of the random fluctuations is consistent with previous observations reported for air path interferometers.[23,24] External to the interferometers the pulse pair travels a common path separated in time by $\tau<200$ ps; since air path fluctuations in these segments are common to both pulses they cancel out in the interference pattern.

Tests on high quality Be ablators (flat) so far revealed that nonuniformities imprinted on the shock front, if present, are at levels at or below the current noise floor, i.e., not detectable with the current instrument. This result was expected because the shock amplitudes exceeded the threshold for shock melting of Be by a significant margin, and detailed modeling suggested that under these conditions the level of nonuniformities should be below the current noise floor. Tests on lower quality Be ablator samples, which included some of the rippled samples tested here, did reveal nonuniformities (the parts of the high frequency spectrum lying slightly above the noise level), but detailed discussion of this is beyond the scope of this article

We are working to improve the noise floor by containing the interferometers within vacuum enclosures. When air-path fluctuations are eliminated, the ultimate noise floor will be determined by photon counting statistics. We have performed a Monte-Carlo study of the counting statistics of the quadrature recording system and find the scaling relation $\delta\phi = 3.1/\sqrt{N}$, where $\delta\phi$ is the statistical phase fluctuation and N is the total number of photons per resolution element (summed over the 4 frames). A CCD with full well capacity of $90000e^-$ (maximum $N \sim 360000$ per pixel) should reach $\delta\phi \sim 5$ mrad or $\sim\lambda/1000$ phase resolution; this limit can be improved by further binning the data at the expense of spatial averaging. This will allow us to reach <1 m/s rms noise, or $\delta V/V < 10^{-4}$ velocity resolution on the 20 km/s shock front in the ICF ablators.

ACKNOWLEDGMENTS

We thank the OMEGA operations staff for their invaluable assistance; special thanks to Jim Cox and Jim Richards of LLNL for help with design, fabrication, and logistics, and to Bob Keck of the OMEGA facility for help with the systems interface. This work was performed under the auspices of the U.S. Department of Energy by Lawrence Livermore National Laboratory under Contract No. DE-AC52-07NA27344.

APPENDIX: VELOCITY SENSITIVITY

We consider the nonuniform motion of a reflecting surface in vacuum. At time t_0 the surface begins to move (e.g., from a shock interacting with a free surface). We define the optical probing direction normal to the surface to be the z-axis. The surface profile expressed as a function of transverse coordinates and time is

$$Z(x,y,t) = Z_0(x,y) + \int_{t_0}^{t} V(x,y,t)dt,$$

where $Z_0(x,y)$ describes the initial surface profile and $V(x,y,t)$ is the velocity of the surface ($V=0$ for $t<t_0$). A pulse of duration τ_p from the probe is directed through the system and detected after traveling through the four available paths. Of the interfering pair of pulses, the first (second) takes the undelayed (delayed) path through the first interferometer to arrive at the target at time t (at time $t+\tau$), returning through the delayed (undelayed) arm of the second interferometer. The optical path difference (OPD) from source to detector of the interfering pair is matched to within several wavelengths, equal to P_0. The OPDs of the remaining two pulses are equal to $P_{-\tau}=P_0-c\tau$ and $P_{+\tau}=P_0+c\tau$ corresponding to the shortest and longest possible paths, respectively (both undelayed arms or both delayed arms, respectively). Since $\tau \gg \tau_p$, these pulses do not produce interference. Owing to the motion of the target the OPDs of the interfering pair of pulses are not precisely equal: there is a net difference given by

$$\Delta P(x,y) = -2(Z(x,y,t+\tau) - Z(x,y,t))$$
$$= -2\left(-\int_{t_0}^{t+\tau} V(x,y,t)dt + \int_{t_0}^{t} V(x,y,t)dt\right)$$
$$= 2\tau\langle V(x,y,t+\tau/2)\rangle|_{\tau}. \quad \text{(A1)}$$

Thus the net path difference is proportional to τ and to the moving average of the local surface velocity averaged over the duration τ, centered at time $t+\tau/2$. For $V\sim 20$ km/s and $\tau\sim 200$ ps one finds $\Delta P\sim 8$ μm (20 fringes). The phase shift displayed by the output interferometer is given by

$$\phi(x,y) = \frac{2\pi}{\lambda}(1+\delta)\Delta P(x,y,t)$$
$$= \frac{4\pi\tau}{\lambda}(1+\delta)\langle V(x,y,t+\tau/2)\rangle|_{\tau}, \quad \text{(A2)}$$

where the extra factor of $(1+\delta)$ is required to account for effect of dispersion in the glass delay etalons[8] (for our fused silica etalons $\delta=0.0568$ at $\lambda=395$ nm). The relationship between phase and velocity of Eq. (A2) is effectively the same expression as given by Eq. (1) in Barker and Hollenbach.[7]. This expression is easily generalized to account for cases where the reflecting surface is embedded within a refracting medium either as a material interface or an ionizing shock front.[12]

[1] P. J. Brannon, C. Konrad, R. W. Morris, E. D. Jones, and J. R. Asay, J. Appl. Phys. **54**, 6374 (1983).
[2] D. E. Grady, Mech. Mater. **29**, 181 (1998).
[3] D. E. Hare, N. C. Holmes, and D. J. Webb, Phys. Rev. B **66**, 014108 (2002).
[4] K. Kadau, T. C. Germann, P. S. Lomdahl, and B. L. Holian, Phys. Rev. B **72**, 064120 (2005).
[5] W. M. Trott, M. R. Baer, J. N. Castaneda, L. C. Chhabildas, and J. R. Asay, J. Appl. Phys. **101**, 024917 (2007).
[6] T. J. Vogler, W. M. Trott, W. D. Reinhart, C. S. Alexander, M. D. Furnish, M. D. Knudson, and L. C. Chhabildas, Int. J. Impact Eng. **35**, 1844 (2008).
[7] L. M. Barker and R. E. Hollenbach, J. Appl. Phys. **43**, 4669 (1972).
[8] L. M. Barker and K. W. Schuler, J. Appl. Phys. **45**, 3692 (1974).
[9] W. F. Hemsing, Rev. Sci. Instrum. **50**, 73 (1979).
[10] W. F. Hemsing, A. R. Mathews, R. H. Warnes, M. J. George, and G. R. Whittemore, in *Shock Compression of Condensed Matter-1991*, edited by S. C. Schmidt, R. D. Dick, J. W. Forbes, and D. G. Tasker (North-Holland, Amsterdam, 1992), pp. 767–770.
[11] K. Baumung, J. Singer, S. Razorenov, and A. Utkin, in *Shock Compression of Condensed Matter-1995*, edited by S. Schmidt and W. Tao (AIP, Woodbury, NY, 1996), p. 1015.
[12] P. M. Celliers, D. K. Bradley, G. W. Collins, D. G. Hicks, T. R. Boehly, and W. J. Armstrong, Rev. Sci. Instrum. **75**, 4916 (2004).
[13] J. Lindl, Phys. Plasmas **2**, 3933 (1995).
[14] S. W. Haan, D. A. Callahan, M. J. Edwards, B. A. Hammel, D. D. Ho, O. S. Jones, J. D. Lindl, B. J. MacGowan, M. M. Marinak, D. H. Munro, S. M. Pollaine, J. D. Salmonson, B. K. Spears, and L. J. Suter, Fusion Sci. Technol. **55**, 227 (2009).
[15] D. J. Erskine and N. C. Holmes, Nature (London) **377**, 317 (1995).
[16] D. J. Erskine and N. C. Holmes, Proc. SPIE **2869**, 1080 (1997).
[17] D. H. Munro, Phys. Fluids B **1**, 134 (1989).
[18] J. W. Bates, Phys. Rev. E **69**, 056313 (2004).
[19] T. R. Boehly, D. L. Brown, R. S. Craxton, R. L. Keck, J. P. Knauer, J. H. Kelly, T. J. Kessler, S. A. Kumpan, S. J. Loucks, S. A. Letzring, F. J. Marshall, R. L. McCrory, S. F. B. Morse, W. Seka, J. M. Soures, and C. P. Verdon, Opt. Commun. **133**, 495 (1997).
[20] The output phase in this data set was slightly contaminated by a ghost reflection from the external surface of the target package which interfered with the reflection from the shock front, because the two surfaces were within the coherence length of the probe pulse. Although the external surface was antireflection coated, such coatings are never perfect, and its contribution is apparent at a residual level. This problem is easily corrected by changing the dimensions of the target package (increasing the thickness of the PMMA layer), and it is not present for reflections from free surfaces.
[21] The peak-to-valley ripple velocity can be estimated as $\delta V = 4\pi c\ \delta A/T \sim 50$ m/s, where $\delta A = 125$ nm is the imposed perturbation amplitude, $T\sim 2.4$ ns is the period, and $c\sim 0.08$ is a coupling factor related to the incident and transmitted shock velocities.
[22] When the expected signal occupies a narrow spectral band (such as the imposed ripple mode) the effective noise floor is obtained by a quadrature summation of the noise spectrum over the spectral components contained within the expected frequency band; thus, the effective noise for the ripple signal quoted above, 1.7 m/s rms or ± 5 m/s peak-to-valley, is smaller than the total rms noise because it occupies only a portion of the spectrum.
[23] N. Bobroff, Appl. Opt. **26**, 2676 (1987).
[24] W. T. Estler, Appl. Opt. **24**, 808 (1985).